

## PAPER • OPEN ACCESS

## Field effect transistors and phototransistors based upon p-type solution-processed PbS nanowires

To cite this article: Paul Giraud *et al* 2018 *Nanotechnology* **29** 075202

View the [article online](#) for updates and enhancements.

## Related content

- [Highly sensitive visible to infrared MoTe<sub>2</sub> photodetectors enhanced by photogating effect](#)  
Hai Huang, Jianlu Wang, Weida Hu et al.
- [Electrical transport and persistent photoconductivity in monolayer MoS<sub>2</sub> phototransistors](#)  
Antonio Di Bartolomeo, Luca Genovese, Tobias Foller et al.
- [Graphene and PbS quantum dot hybrid vertical phototransistor](#)  
Xiaoxian Song, Yating Zhang, Haiting Zhang et al.



**IOP | ebooks™**

Bringing you innovative digital publishing with leading voices to create your essential collection of books in STEM research.

Start exploring the collection - download the first chapter of every title for free.

# Field effect transistors and phototransistors based upon p-type solution-processed PbS nanowires

Paul Giraud<sup>1,3</sup> , Bo Hou<sup>1,3</sup> , Sangyeon Pak<sup>1</sup>, Jung Inn Sohn<sup>1</sup> , Stephen Morris<sup>1</sup>, SeungNam Cha<sup>1</sup>  and Jong Min Kim<sup>2</sup>

<sup>1</sup>Department of Engineering Science, University of Oxford, Oxford OX1 3PJ, United Kingdom

<sup>2</sup>Department of Engineering, University of Cambridge, Cambridge CB3 0FA, United Kingdom

E-mail: [seungnam.cha@eng.ox.ac.uk](mailto:seungnam.cha@eng.ox.ac.uk)

Received 29 November 2017, revised 15 December 2017

Accepted for publication 19 December 2017

Published 11 January 2018



CrossMark

## Abstract

We demonstrate the fabrication of solution processed highly crystalline p-type PbS nanowires via the oriented attachment of nanoparticles. The analysis of single nanowire field effect transistor (FET) devices revealed a hole conduction behaviour with average mobilities greater than  $30 \text{ cm}^2 \text{ V}^{-1} \text{ s}^{-1}$ , which is an order of magnitude higher than that reported to date for p-type PbS colloidal nanowires. We have investigated the response of the FETs to near-infrared light excitation and show herein that the nanowires exhibited gate-dependent photo-conductivities, enabling us to tune the device performances. The responsivity was found to be greater than  $10^4 \text{ A W}^{-1}$  together with a detectivity of  $10^{13}$  Jones, which benefits from a photogating effect occurring at negative gate voltages. These encouraging detection parameters are accompanied by relatively short switching times of 15 ms at positive gate voltages, resulting from a combination of the standard photoconduction and the high crystallinity of the nanowires. Collectively, these results indicate that solution-processed PbS nanowires are promising nanomaterials for infrared photodetectors as well as p-type nanowire FETs.

Supplementary material for this article is available [online](#)

Keywords: nanowire FET, PbS, colloidal synthesis, p-type nanowires, phototransistor, photodetector

(Some figures may appear in colour only in the online journal)

## Introduction

For a number of years, semiconductor nanowires (NWs) have been widely investigated for their potential deployment in future electronics and optoelectronics technologies [1]. Their large aspect ratio, typically of the order of a few micrometres in length for diameters of around 100 nm, makes them an interesting tool with which to investigate the nanoscale properties of materials. Furthermore, they show outstanding crystalline properties and they enable the fabrication of nanoscale devices without the need for sophisticated patterning processes. As such, a range of promising devices

including field effect transistors (FETs) [2], logic circuits [3], sensors [4], and photodetectors [5] have been demonstrated. With the advent of bottom-up fabrication methods such as vapour-liquid-solid synthesis [6–8], there has been a surge in NW research because these methods allowed for the large-scale synthesis of NWs with diameters beyond the limits of conventional lithography. However, these vapour-phase synthetic procedures require high growth temperatures accompanied by a precise control of the pressure or flow of the reaction gases, which may ultimately impede the large-scale production of NWs and potential commercial applications. Therefore, the research focus has shifted towards cheaper and more facile approaches involving the growth of the NWs from a liquid phase. For such methodologies, NWs

<sup>3</sup> These authors contributed equally to this work.



are either grown out of a metallic seed catalyst (e.g. solution–liquid–solid growth) [9] or out of the oriented attachment of nanoparticles (e.g. colloidal synthesis) [10–12]. NWs can then be readily recovered from the solutions and deployed into various devices through cost-effective processes such as spin coating/casting [13], spray deposition [14] and doctor blading methods [15].

Solution-processed NWs are typically grown from inorganic II–VI and IV–VI semiconductors following a synthesis technique that is similar to that employed for the fabrication of colloidal quantum dots (QDs) [16]. Among them, lead chalcogenides (PbX, X = S, Se, Te) have shown particular promise for optoelectronics applications due to their extensive band gap tunability [17] and earth-abundant availability. Lead sulphide (PbS), for example, is a narrow band gap ( $E_g = 0.41$  eV) semiconductor that has been extensively studied in its QD form for infrared electronics [18–21] and light harvesting [22–24] applications. In addition, the solution processing of PbS nanomaterials has been used to synthesise complex geometrical structures such as hyperbranched NWs [25] or star shaped nanocrystals (NCs) [26]. However, even though the colloidal processing of PbS NWs has been reported a number of times [27, 28], a detailed analysis of their optoelectronic performance still remains unexplored. Furthermore, p-type NWs are known to be notoriously more difficult to produce than their n-type counterparts [29]. Therefore, there is still a need for a facile procedure for fabricating p-type NWs that result in good device performance metrics such as large majority carrier field effect mobility and large ON to OFF current ratios.

In this work, we have successfully fabricated single crystalline PbS NWs using solution processing and have employed them in single NW FET devices. Even though the device fabrication and measurements were made in ambient conditions, our NWs are found to exhibit stable hole conduction (p-type semiconductor) with high field effect mobilities that are, on average, larger than  $31.6 \text{ cm}^2 \text{ V}^{-1} \text{ s}^{-1}$ , but that can reach values as high as  $166 \text{ cm}^2 \text{ V}^{-1} \text{ s}^{-1}$  for champion devices. To evaluate the potential application of PbS NWs in infrared-related technologies, NW phototransistors were made and their response to an 850 nm light source was evaluated. It was found that different photoconductive mechanisms occurred, enabling high photoresponsivity and fast response times by simply tuning the gate voltage.

## Experimental details

### *PbS nanowire synthesis*

The colloidal synthesis of the PbS NWs follows an oriented attachment process [16]. Using this technique, NWs are grown by first synthesising NCs of PbS via a hot-injection process [30], which then combine along energetically favourable faces [31]. By tuning parameters such as the precursor concentration, temperature and reaction time, it is possible to adjust the dimensions of the nanomaterials, making the process extremely versatile [24]. The PbS seed-solution was prepared by a mixture

of lead oleate with trioctylphosphine coordinated sulphur (TOPS). These precursors were swiftly injected into a diphenyl ether solution (ca  $T = 250$  °C) to initialise the oriented attachment growth of PbS NWs. The NWs were then recovered by centrifugation at 8000 rpm for 10 min from an acetone/hexane mixture solution (1:1/V:V). Specifically, 0.3207 g of sulphur was dissolved in 10 ml of trioctylphosphine (TOP) for 2 h at 50 °C to form the sulphur precursor (TOPS). In parallel, 0.76 g of lead acetate trihydrate and 2 ml of oleic acid were dissolved in 10 ml of diphenyl ether to form the lead precursor. After cooling to 60 °C, the lead oleate solution was mixed with 4 ml of 0.668 mol (0.668 ml, 1.0 M TOPS) TOPS solution in TOP and injected under vigorous stirring into a hot (250 °C) solution containing 0.2 g of n-tetradecylphosphonic acid dissolved in 15 ml of diphenyl ether. After 5 min of heating, the reaction mixture was quenched to room temperature using a water bath. When not used for measurement purposes, the NWs were stored in dark conditions in a toluene solution and argon-sealed vials.

### *Device fabrication and measurements*

Photolithography was used to deposit a combination of 5/45 nm of titanium/gold interdigitated electrodes onto a highly p-doped silicon substrate, covered by a thermally grown layer of 3000 Å silicon dioxide (SiO<sub>2</sub>). The electrode spacing was 5 μm. A few drops (~0.2 ml) from a diluted solution of PbS NWs were subsequently spin-cast at 2000 rpm for 30 s. Finally, a large amount of methanol was spin-cast onto the devices to ensure the sufficient removal of the excess of ligands (10 drops, 30 s, two times). The gold electrodes formed an ohmic contact with PbS NWs without any further treatment (figure S1 is available online at [stacks.iop.org/NANO/29/075202/mmedia](https://stacks.iop.org/NANO/29/075202/mmedia)). All the devices that were fabricated were stored in ambient room conditions. Transfer curves and output curves were measured in dark and ambient conditions (air and room temperature) using a probe station together with a Keithley 4200-SCS parameter analyser. Photodetection measurements were made using an 850 nm near-infrared (NIR) laser source (Roithner Laser-Technik LDM850/3LJ) that was externally triggered by a waveform generator (LeCroy WaveStation 2012). The time response was measured using a digital oscilloscope (Teledyne HDO4104) reading a signal that was pre-amplified by an I/V converter (Stanford SR570). When required, an external gate bias voltage was applied with the aid of a DC power supply (Kikusui PWR400H).

## Results and discussion

Transmission electron microscopy (TEM) and high-resolution TEM (HRTEM) were employed to characterise the morphology of the as-grown PbS NWs. The results showed that the NWs had diameters within the range of 30–60 nm and were as long as 10 μm, which is a favourable aspect ratio in terms of device fabrication. Figure 1(a) shows that the NWs have rough, zigzag-shaped edges, which is similar to the

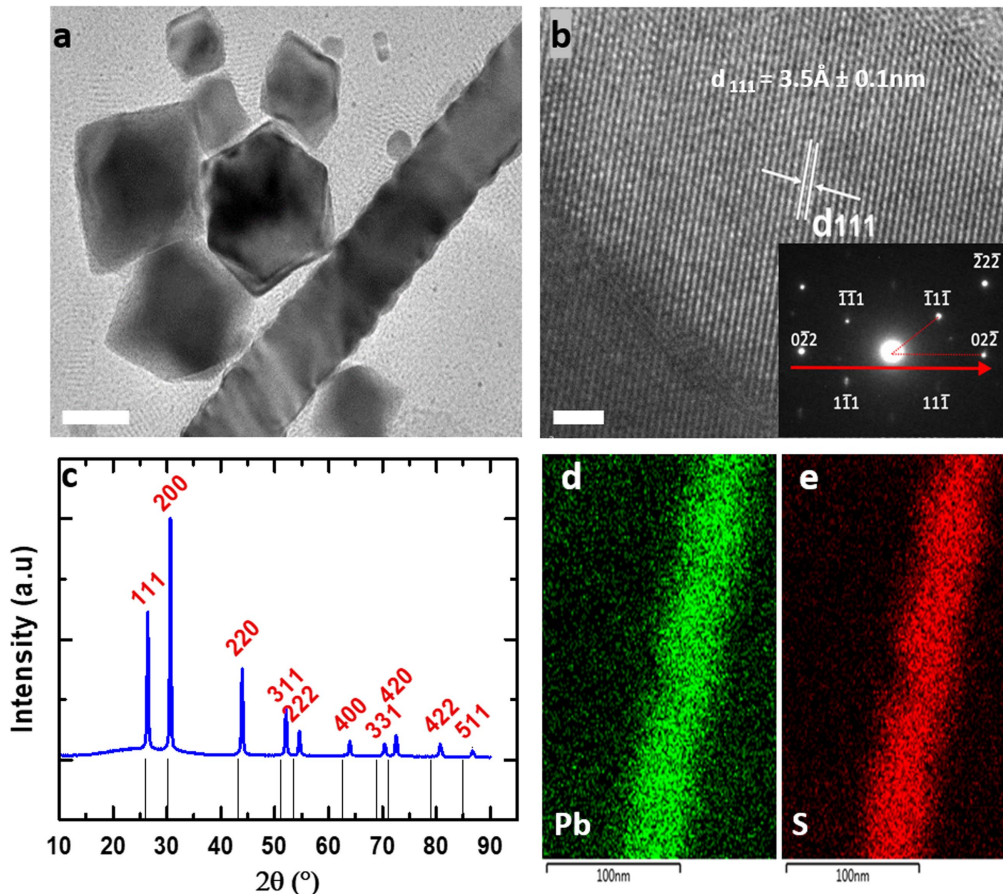


**Figure 1.** (a) TEM image of a 50 nm diameter PbS NW. Scale bar = 50 nm. (b) HRTEM image of the NW surface. Scale bar = 2 nm. The  $d_{111}$  crystalline planes with 3.5 Å spacing, which matches that of bulk PbS, can be readily observed. SAED pattern (inset, zone axis  $= [011]$ ) confirms the  $[110]$  growth direction). (c) XRD pattern of the PbS NWs (top, blue) and of bulk PbS (bottom lines, black) from PDF—78 1057. (d), (e) high angle annular dark field STEM-energy-dispersive x-ray spectrometry element mappings of the as-prepared PbS NWs. Scale bar = 100 nm.

observations made by Jang *et al* [27]. Octahedral shaped NCs can also be seen, which are the residues of the PbS seeds that did not take part in the oriented attachment process that formed the resultant NWs. In the HRTEM image depicted in figure 1(b), the  $\{111\}$  crystal planes are clearly observed and reveal the high degree of crystallinity of the as-prepared NWs. It is shown that the  $\{111\}$  planes are separated by a distance of 3.5 Å, which is in accordance with that observed for bulk PbS (Power Diffraction File PDF—78 1057).

The x-ray diffraction (XRD) pattern of the as-synthesised NWs is presented in figure 1(c). It is found that the peaks closely match the XRD pattern obtained for bulk PbS (PDF—78 1057) indicating that the lead and sulphide atoms are arranged in a rock-salt-like cubic structure with a high degree of crystallinity. The slight displacements of the measured XRD peaks compared to the standard bulk PDF values are due to the presence of the glass substrate used during the measurements. Indeed, the rock-salt galena cubic configuration can be readily indexed from the selected area electron diffraction (SAED) image (figure 1(b), inset). The SAED pattern was captured along the  $[011]$  zone axis which further confirms the single crystal nature of the NWs and indicates that growth took place along the  $[110]$  direction. To gain

insight into the surface composition, we performed high angle annular dark field scanning transmission electron microscopy analysis together with element mapping, which confirmed that both lead (figure 1(d)) and sulphide (figure 1(e)) were present on the NW surface. A quantitative energy-dispersive x-ray spectrometry (EDX) analysis (figure S3) revealed that the as-prepared PbS NWs were predominantly lead-rich.

The as-grown NWs were spin-coated onto a doped silicon substrate covered by a layer of silicon dioxide (300 nm) onto which Cr/Au electrodes had already been patterned using standard photolithography techniques. Devices were thoroughly cleaned in methanol to ensure the removal of the excess organic ligands that originated from the synthesis procedure. A high-resolution SEM image of a single PbS NW FET is shown in figure 2(a). Atomic force microscopy imaging (figure 2(a), inset) reveals that the nanowire bends quite considerably at the electrode interface, implying good mechanical flexibility. It also shows that most of the NW, and therefore the FET channel, is in contact with the underlying  $\text{SiO}_2$  dielectric layer. The transistor drain-source current  $I_{ds}$  was measured as a function of the bias voltage  $V_{ds}$  for different gate voltages,  $V_g$  and the corresponding output curves are presented in figure 2(b). It is shown that  $I_{ds}$  evolves



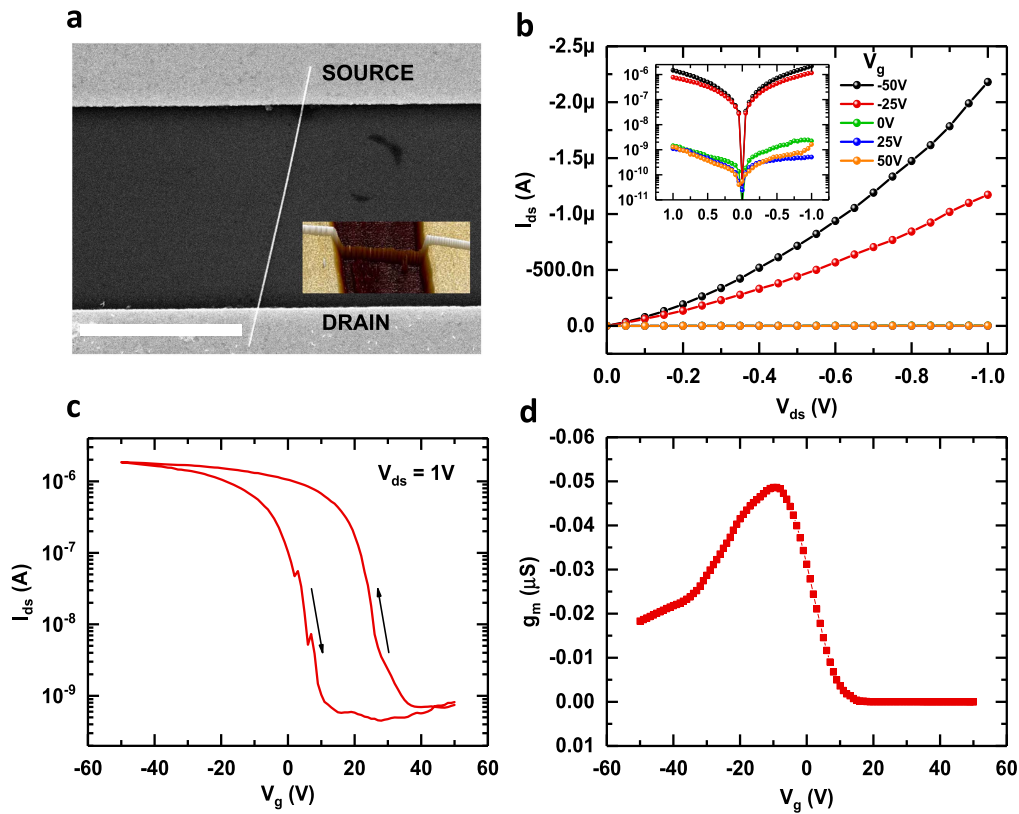


**Figure 2.** (a) SEM image of a bottom contact, single NW PbS FET. Scale bar = 5  $\mu\text{m}$ . The measured diameter of the NW is 53 nm. The AFM inset shows the mechanical bending of the NW at the electrode contacts. (b) Output  $I_{ds}$  curves of a PbS NW for gate voltages ranging from  $-50$  V (black) to  $50$  V (orange), in  $25$  V increments. The inset shows the same plot on a log-scale. (c) Transfer curve of the same PbS NW device; the hysteresis was evaluated by performing first a forward sweep on the gate voltage (i.e. from  $50$  to  $-50$  V for p-type FETs) followed by a reverse sweep ( $-50$  to  $50$  V). (d) Corresponding transconductance plot for  $g_m$  defined as  $g_m = \frac{dI_{ds}}{dV_g}$  (reverse sweep).

linearly for low  $V_{ds}$ , showing that ohmic contacts are formed at the PbS/Au interface. It is also shown that  $I_{ds}$  decreases with increasing values of  $V_g$ , confirming the p-type semiconducting nature of our PbS NWs in accordance with previous results reported in the literature [27, 32–35]. The p-type nature of lead chalcogenide structures has been reported to be the result of either a stoichiometric imbalance, where the amount of chalcogen atoms (S, Se) exceeds those of lead [32], or due to oxygen adsorption at the NW surface [36–38]. EDX measurements revealed that the NW surface tended to be lead-rich (figure S3), which leads us to favour the latter hypothesis, as device fabrication, storage and electrical measurements were performed under ambient conditions. The field effect mobility of the NWs could be deduced from the transconductance relationship,  $g_m = \frac{dI_{ds}}{dV_g}$ , which was extracted from the transfer curve (figure 2(d)). Detailed mobility calculations are reported in the supplementary information.

To ensure the reproducibility of the device performances, we carried out a statistical analysis of 53 FETs made with NWs from different batches. The average hole-field effect mobility was found to be  $31.6 \pm 4.78 \text{ cm}^2 \text{ V}^{-1} \text{ s}^{-1}$  for an ON–OFF current ratio of  $1.8 \times 10^3 \pm 518$ . The best performing devices exhibited mobilities as high as  $166 \text{ cm}^2 \text{ V}^{-1} \text{ s}^{-1}$  and a  $10^4$  ON–OFF ratio, suggesting that the device performances could be further improved. These are the

highest values reported so far for solution-processed PbS NWs [27, 28], which compare well with that of solution-based PbSe NWs [39] and is close to the performance of PbS NWs grown via chemical vapour deposition (CVD) [32]. The large hole mobility values place PbS NWs in the upper range in terms of performance of p-type solution-processed NWs [29, 40–42]. Furthermore, these results were obtained after one month of storage in ambient conditions, indicating that they have good air stability properties. In parallel, devices stored in an argon glove box were found to exhibit a hole mobility of  $62.3 \pm 15.0 \text{ cm}^2 \text{ V}^{-1} \text{ s}^{-1}$  and an ON–OFF current ratio of  $2.2 \times 10^3 \pm 558.6$  (12 devices tested). Both storage conditions resulted in devices with similar performances and it can therefore be concluded that the ambient storage conditions did not significantly alter the performance of the resultant FETs. Interestingly, an increase in the ON–OFF ratio of the NWs was observed following aging in both argon and ambient storage conditions and they were found to reach a stable condition after three to four weeks<sup>4</sup>. A gate hysteresis effect can also be observed in figure 2(c), which is attributed to the measurement performed under ambient conditions. Indeed, it is known that for one-

<sup>4</sup> The results presented here are therefore from devices at least a month old to ensure consistency. Figures showing the effect of aging on the ON–OFF ratio are presented in the supplementary information.

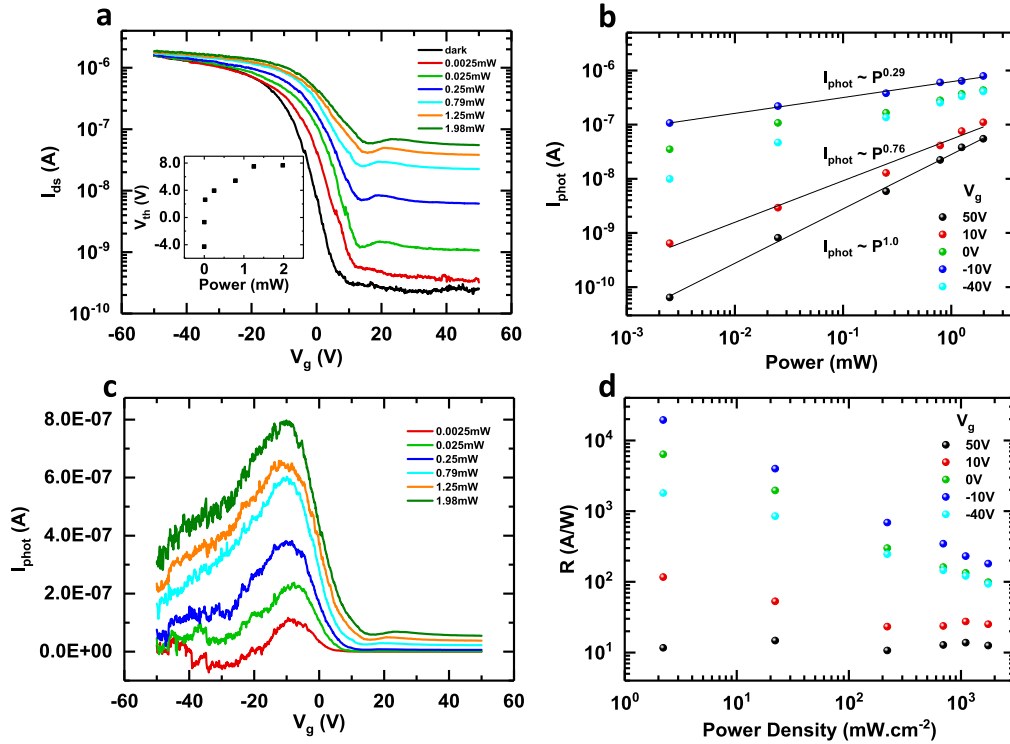


**Figure 3.** (a) Transfer curves of a device measured under illumination with 850 nm laser light at different power densities. The inset shows the threshold voltage,  $V_{th}$ , as a function of the incident power. (b) Power dependence of the photocurrent,  $I_{phot}$  at different gate voltages. (c) Photocurrent  $I_{light}-I_{dark}$  as a function of gate-voltage extracted from (a). The negative photocurrent observed at  $V_g = -30$  V and  $P = 0.0025$  mW is discarded as an uncertainty in the measurement. (d) Gate-dependent photoresponsivities,  $R$ , extracted from the data plotted in (b).

dimensional FETs, water and oxygen molecules at the semiconductor/dielectric interface can induce charges that screen out the gate electric field, which can, in turn, lead to a hysteresis in the plots [43, 44]. FET parameters such as sub-threshold swing ( $4.4$  V  $\text{dec}^{-1}$ ), threshold voltage ( $2.5$  V) and free-carrier concentration ( $3.1 \times 10^{17} \text{ cm}^{-3}$ ,  $n_p = \frac{C V_{th}}{q \pi r^2 L}$ ) can also be extracted from the transfer characteristics (figure 2(c)).

To demonstrate the potential use of PbS NWs for optoelectronic applications, the response of the devices to an 850 nm NIR laser diode was evaluated. Figure 3(a) shows the phototransistor transfer curves measured at various incident powers. A prime advantage of the phototransistor configuration is that the field effect modulation allows for low currents in the transistor OFF-state, which boosts the light response while reducing the dark current noise (shot noise). The photocurrent as a function of the laser power  $P$  was subsequently extracted and fitted with a power law dependence,  $I_{phot} \sim P^\alpha$ . As can be seen in figure 3(b), the photocurrent exhibits different behaviour depending on the gate voltage. Indeed, for positive gate voltages, corresponding to the OFF-state of the transistor, the exponent  $\alpha$  is found to be close to unity, implying that the photocurrent scales linearly with increasing incident power. However, when going to the ON-state (i.e. negative gate voltages),  $\alpha$  decreases to 0.36 and the photocurrent scales sub-linearly with the power. The different gate-dependent behaviour implies that two different photogeneration mechanisms occur in the NW. In the OFF-state, the linear  $I_{phot} \sim P$  behaviour is characteristic of the standard

photoconductive effect, where photogenerated charges increase the free-carrier concentration in the channel and hence the drain current [45]. On the other hand, in the ON-state the carrier concentration is saturated as indicated by the decrease in the transconductance shown in figure 2(d). Therefore, photogenerated carrier contribution to the current is limited and a photogating effect dominates.

Photogating is due to the long lifetime trapping of photogenerated carriers in localised states near the band edges, which results in a shift of the Fermi level within the semiconductor [46, 47]. The photocurrent induced by photogating is proportional to the transconductance  $g_m$  and can be expressed as  $I_{pg} = g_m \Delta V_{th}$  [45], where  $\Delta V_{th}$  is the variation in the threshold voltage due to a shift in the Fermi level. The shift in  $V_{th}$  is plotted in the inset of figure 3(a) and clearly scales nonlinearly with the power of the incident light [45]. The direction of the shift towards positive voltages indicates that electrons become pinned within the so-called trap states, which are believed to be due to interactions between oxygen and the surface of the NW as well as interface states that arise from direct contact with the dielectric oxide. Konstantatos *et al* reported the existence of long lifetime electron trap states in PbS QDs due to the presence of surface lead oxides ( $\text{PbSO}_4$ ,  $\text{PbSO}_3$ ) and lead carboxylates [48], which could very well be present in our NWs due to the similarities in the device fabrication and nanomaterial synthesis that have been implemented. The proportionality of the photogating current  $I_{pg}$  with the transconductance is evidenced in figure 3(c)

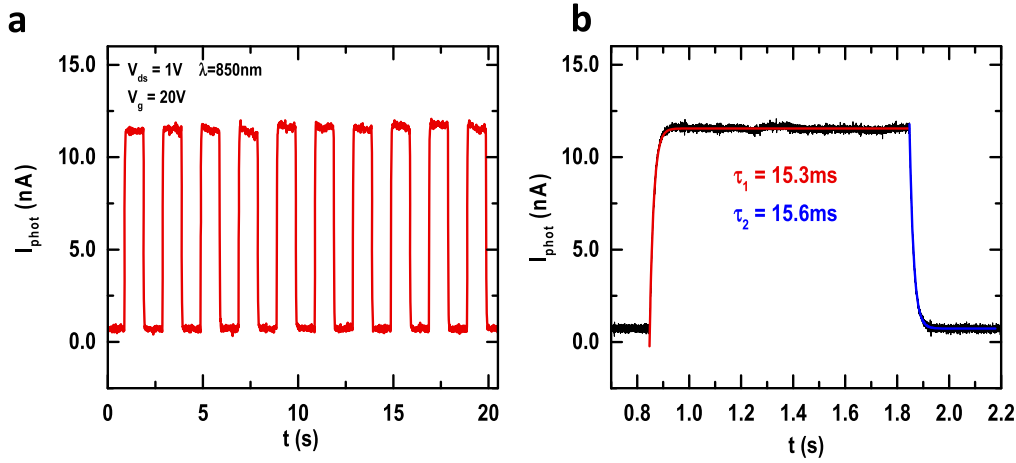


**Figure 4.** (a) Dynamic response of a PbS NW FET in the OFF-state to an 850 nm laser pulsed at a frequency of 500 mHz. (b) A magnified plot of one of the crenels shown in (a). The red and blue lines are exponential fits that were used to determine the rise,  $\tau_1$ , and fall times  $\tau_2$ , respectively.

where the photocurrent measured at different power densities evolves in a similar fashion to the transconductance plotted in figure 2(d).

To quantify the response of the NW to incident light, we have calculated the photoresponsivity,  $R$ , using the relation

$$R = \frac{I_{\text{phot}}}{P_d A_{\text{eff}}}, \quad (1)$$

where  $A_{\text{eff}}$  is the NW effective area, approximated to be  $2.5 \times 10^{-9} \text{ cm}^2$  for each device (50 nm diameter, 5  $\mu\text{m}$  long NWs), and  $P_d$  is the laser power density, which was calculated by dividing the total power by the laser spot size<sup>5</sup>. From this, the normalised detectivity,  $D^*$ , of the photodetector  $D^* = R(A_{\text{eff}} B)^{1/2} / i_n$  could also be determined, where  $B$  is the electrical bandwidth and  $i_n$  is the shot noise current, defined as  $i_n = (2qI_{\text{dark}} B)^{1/2}$ , with  $q$  representing the electron charge. The power dependent photoresponsivity of the device presented in figure 3(a) is shown in figure 3(c) for various gate voltages. In this exemplar device, the responsivity is found to reach a maximum value of  $1.9 \times 10^4 \text{ A W}^{-1}$ , which was obtained at the peak of the transconductance ( $V_g = -10 \text{ V}$ ), a power density of  $2 \text{ mW cm}^{-2}$ , a gate voltage of  $-10 \text{ V}$  and a drain bias of  $-1 \text{ V}$ . The corresponding value of  $D^*$  was then calculated to be  $1.9 \times 10^{13}$  Jones. These performance metrics are comparable to other NW photodetectors such as cadmium sulphide (CdS) or indium arsenide (InAs) [47, 49]. At positive gate voltages, the transconductance is both constant and minimal (figure 2(d)), resulting in a decrease in the photogating effect as the regular photoconduction becomes dominant. Therefore, the photocurrent becomes independent of the gate voltage and the measured responsivity was found to be of the order of  $10 \text{ A W}^{-1}$  ( $D^* \approx 10^{11}$  Jones).

<sup>5</sup> The spot size was measured using a CCD camera set up and taken to be 380  $\mu\text{m}$ . A knife-edge measurement, with a laser to detector distance equal to the laser to device distance within the probe station, (millimetre precision) and with the same laser focus, gave similar spot size values.

Finally, we investigated the time response of the NW phototransistor to a NIR laser pulse (850 nm,  $P = 2.5 \text{ mW}$ ) as shown in figure 4(a). The photocurrent was measured in the transistor OFF-state, for another exemplar device, whose transfer curves in the dark and under illumination conditions can be found in figure S5. By evaluating the time response in the OFF-state, where the photoconduction mechanism is dominant, the influence of the trap recombination centres is minimised and thus the response times are found to be shorter. The time response was measured after a short reset in the ON-state to account for any hysteresis. The time constants of the photoconductor corresponding to the rise,  $\tau_1$ , and fall times,  $\tau_2$ , were extracted from exponential fits of the form  $y = y_0 + A_1 \cdot \exp\left(\frac{x - x_0}{\tau}\right)$  (figure 4(b)). The rise and fall times, which were found to be 15.3 ms and 15.6 ms, respectively, were obtained at a bias voltage of 1 V and are clearly very similar. It is noted that the switching times of our phototransistors are much faster than that reported for PbSe NW-based photoconductors whose time response has been reported to be of the order of a few seconds [39] and comparable to previously reported CVD-grown PbS NWs [33, 50]. Beside the fact that in the OFF-state the trapping effects are limited, we also attribute these good device parameters to the high degree of crystallinity of our NWs, which has previously been shown to enhance the performances of nanostructured photodetectors [51].





In summary, solution-processed colloidal PbS NWs that are up to 10  $\mu\text{m}$  in length and around 50 nm in diameter have been successfully synthesised. XRD and TEM analysis indicated that the colloidal synthesis allows for the fabrication of NWs with a high degree of crystallinity. Single NW FETs revealed that the NWs are predominantly p-type in behaviour, exhibiting a record hole-mobility of  $166 \text{ cm}^2 \text{ V}^{-1} \text{ s}^{-1}$ . The transfer curves exhibited gate-dependent hysteresis which was attributed to both localised surface states that were formed at the NW/dielectric interface and to structural defects. Nonetheless, the devices showed excellent stability and could be stored in ambient conditions for many weeks without a

significant alteration in their performance. Subsequently, we studied the response of the phototransistors to incident light and the devices showed gate-tunable photo-conductivities with a high photoresponsivity in the ON-state due to a photogating effect as well as fast response times in the transistor OFF-state. The best device in terms of performance was found to have a responsivity and normalised detectivity of  $1.9 \times 10^4 \text{ A W}^{-1}$  and  $1.9 \times 10^{13}$  Jones, respectively, occurring in the linear regime of the field effect modulation. In the transistor OFF-mode, where a simple, gate-independent, photoconduction mechanism is dominant, fast switching times of the order of 15 ms were obtained. These high-performance metrics make solution-processed PbS NWs an exciting material for infrared optoelectronics such as thermal imaging and, more broadly, a functional and economical p-type NW.

## Acknowledgments

This research was supported by the European Research Council under the European Union's Seventh Framework Programme (FP/2007-2013)/Grant Agreements 340538 (Project 'UniQDS'), 685758 (Project '1D-NEON') and National Research Foundation (NRF) of Korea (2015M2A2A6A02045252). In addition, S M M would also like to thank The Royal Society for financial support.

## ORCID iDs

Paul Giraud  <https://orcid.org/0000-0002-1052-9202>  
 Bo Hou  <https://orcid.org/0000-0001-9918-8223>  
 Jung Inn Sohn  <https://orcid.org/0000-0002-3155-4327>  
 SeungNam Cha  <https://orcid.org/0000-0001-6284-8312>

## References

- [1] Dasgupta N P, Sun J, Liu C, Brittan S, Andrews S C, Lim J, Gao H, Yan R and Yang P 2014 25th anniversary article: semiconductor nanowires—synthesis, characterization, and applications *Adv. Mater.* **26** 2137–84
- [2] Duan X, Huang Y, Cui Y, Wang J and Lieber C M 2001 Indium phosphide nanowires as building blocks for nanoscale electronic and optoelectronic devices *Nature* **409** 66–9
- [3] Huang Y 2001 Logic gates and computation from assembled nanowire building blocks *Science* **294** 1313–7
- [4] Wan Q, Li Q H, Chen Y J, Wang T H, He X L, Li J P and Lin C L 2004 Fabrication and ethanol sensing characteristics of ZnO nanowire gas sensors *Appl. Phys. Lett.* **84** 3654–6
- [5] Soci C, Zhang A, Bao X-Y, Kim H, Lo Y and Wang D 2010 Nanowire photodetectors *J. Nanosci. Nanotechnol.* **10** 1430–49
- [6] Klimov V I, Mikhailovsky A A, Xu S, Malko A, Hollingsworth J A, Leatherdale C A, Eisler H, Bawendi M G and Yang P 2000 Optical gain and stimulated emission in nanocrystal quantum dots *Science* **290** 314–7
- [7] Gudixsen M S, Lauhon L J, Wang J, Smith D C and Lieber C M 2002 Growth of nanowire superlattice structures for nanoscale photonics and electronics *Nature* **415** 617–20
- [8] Yang P, Yan H, Mao S, Russo R, Johnson J, Saykally R, Morris N, Pham J, He R and Choi H-J 2002 Controlled growth of ZnO nanowires and their optical properties *Adv. Funct. Mater.* **12** 323
- [9] Wang F, Dong A, Sun J, Tang R, Yu H and Buhro W E 2006 Solution–liquid–solid growth of semiconductor nanowires *Inorg. Chem.* **45** 7511–21
- [10] Zhang H et al 2014 Interatomic Coulombic interactions as the driving force for oriented attachment *CrystEngComm* **16** 1568–78
- [11] Xue X et al 2014 Crystal growth by oriented attachment: kinetic models and control factors *CrystEngComm* **16** 1419
- [12] Talapin D V, Black C T, Kagan C R, Shevchenko E V, Afzali A and Murray C B 2007 Alignment, electronic properties, doping, and on-chip growth of colloidal PbSe nanowires *J. Phys. Chem. C* **111** 13244–9
- [13] Liang W, Rabin O, Hochbaum A I, Fardy M, Zhang M and Yang P 2010 Thermoelectric properties of p-type PbSe nanowires *Nano Res.* **2** 394–9
- [14] Scardaci V, Coull R, Lyons P E, Rickard D and Coleman J N 2011 Spray deposition of highly transparent, low-resistance networks of silver nanowires over large areas *Small* **7** 2621–8
- [15] Krantz J, Richter M, Spallek S, Spiecker E and Brabec C J 2011 Solution-processed metallic nanowire electrodes as indium tin oxide replacement for thin-film solar cells *Adv. Funct. Mater.* **21** 4784–7
- [16] Cho K-S, Talapin D V, Gaschler W and Murray C B 2005 Designing PbSe nanowires and nanorings through oriented attachment of nanoparticles *J. Am. Chem. Soc.* **127** 7140–7
- [17] Moreels I, Justo Y, De Geyter B, Haustraete K, Martins J C and Hens Z 2011 Size-tunable, bright, and stable PbS quantum dots: a surface chemistry study *ACS Nano* **5** 2004–12
- [18] Saran R and Curry R J 2016 Lead sulphide nanocrystal photodetector technologies *Nat. Photon.* **10** 81–92
- [19] Konstantatos G and Sargent E H 2007 PbS colloidal quantum dot photoconductive photodetectors: transport, traps, and gain *Appl. Phys. Lett.* **91** 173505
- [20] Konstantatos G, Badioli M, Gaudreau L, Osmond J, Bernechea M, Garcia de Arquer F P, Gatti F and Koppens F H L 2012 Hybrid graphene-quantum dot phototransistors with ultrahigh gain *Nat. Nanotechnol.* **7** 363–8
- [21] Kufer D, Nikitskiy I, Lasanta T, Navickaite G, Koppens F H L and Konstantatos G 2015 Hybrid 2D–0D MoS<sub>2</sub>–PbS quantum dot photodetectors *Adv. Mater.* **27** 176–80
- [22] Chuang C-H M, Brown P R, Bulović V and Bawendi M G 2014 Improved performance and stability in quantum dot solar cells through band alignment engineering *Nat. Mater.* **13** 796–801
- [23] Cho Y et al 2017 Charge transport modulation of a flexible quantum dot solar cell using a piezoelectric effect *Adv. Energy Mater.* **accepted** 1700809
- [24] Hou B, Cho Y, Kim B S, Hong J, Park J B, Ahn S J, Sohn J I, Cha S and Kim J M 2016 Highly monodispersed PbS quantum dots for outstanding cascaded-junction solar cells *ACS Energy Lett.* **1** 834–9
- [25] Patla I, Acharya S, Zeiri L, Israelachvili J, Efrima S and Golan Y 2007 Synthesis, two-dimensional assembly, and surface pressure-induced coalescence of ultranarrow PbS nanowires *Nano Lett.* **7** 1459–62
- [26] Pawar M S, Bankar P K, More M A and Late D J 2017 PbS nanostar-like structures as field emitters *ChemistrySelect* **2** 5175–9



- [27] Jang S Y *et al* 2010 Three synthetic routes to single-crystalline PbS nanowires with controlled growth direction and their electrical transport properties *ACS Nano* **4** 2391–401
- [28] Loc W S *et al* 2015 Facet-controlled facilitation of PbS nanoarchitectures by understanding nanocrystal growth *Nanoscale* **7** 19047–52
- [29] Stoesser A, von Seggern F, Purohit S, Nasr B, Kruk R, Dehm S, Wang D, Hahn H and Dasgupta S 2016 Facile fabrication of electrolyte-gated single-crystalline cuprous oxide nanowire field-effect transistors *Nanotechnology* **27** 415205
- [30] Hou B *et al* 2017 Red green blue emissive lead sulfide quantum dots: heterogeneous synthesis and applications *J. Mater. Chem. C* **5** 3692–8
- [31] Schliehe C *et al* 2010 Ultrathin PbS sheets by two-dimensional oriented attachment *Science* **329** 550–3
- [32] Yang Y, Li J, Wu H, Oh E and Yu D 2012 Controlled ambipolar doping and gate voltage dependent carrier diffusion length in lead sulfide nanowires *Nano Lett.* **12** 5890–6
- [33] Graham R, Miller C, Oh E and Yu D 2011 Electric field dependent photocurrent decay length in single lead sulfide nanowire field effect transistors *Nano Lett.* **11** 717–22
- [34] Yang Y, Peng X and Yu D 2014 High intensity induced photocurrent polarity switching in lead sulfide nanowire field effect transistors *Nanotechnology* **25** 195202
- [35] Lee S, Noh J-S, Kim J, Kim M, Jang S Y, Park J and Lee W 2013 The optoelectronic properties of PbS nanowire field-effect transistors *IEEE Trans. Nanotechnol.* **12** 1135–8
- [36] Rogacheva E, Tavrina T, Nashchekina O, Grigorov S, Sipatov A Y, Volobuev V, Dresselhaus M and Dresselhaus G 2003 Influence of oxidation on the transport properties of IV–VI-thin films *Physica E* **17** 310–2
- [37] Rogacheva E I, Krivulkin I M, Nashchekina O N, Sipatov A Y, Volobuev V V and Dresselhaus M S 2001 Effect of oxidation on the thermoelectric properties of PbTe and PbS epitaxial films *Appl. Phys. Lett.* **78** 1661
- [38] Kim D K, Lai Y, Vemulkar T R and Kagan C R 2011 Flexible, low-voltage, and low-hysteresis PbSe nanowire field-effect transistors *ACS Nano* **5** 10074–83
- [39] Oh S J, Uswachoke C, Zhao T, Choi J-H, Diroll B T, Murray C B and Kagan C R 2015 Selective p- and n-doping of colloidal PbSe nanowires to construct electronic and optoelectronic devices *ACS Nano* **9** 7536–44
- [40] Pradel K C, Wu W, Zhou Y, Wen X, Ding Y and Wang Z L 2013 Piezotronic effect in solution-grown p-type ZnO nanowires and films *Nano Lett.* **13** 2647–53
- [41] Tang J *et al* 2010 Single-crystalline Ni<sub>2</sub>Ge/Ge/Ni<sub>2</sub>Ge nanowire heterostructure transistors *Nanotechnology* **21** 505704
- [42] Li G A, Wang C Y, Chang W C and Tuan H Y 2016 Phosphorus-rich copper phosphide nanowires for field-effect transistors and lithium-ion batteries *ACS Nano* **10** 8632–44
- [43] Kim W, Javey A, Vermesh O, Wang Q, Li Y and Dai H 2003 Hysteresis caused by water molecules in carbon nanotube field-effect transistors *Nano Lett.* **3** 193–8
- [44] Aguirre C M, Levesque P L, Paillet M, Lapointe F, St-Antoine B C, Desjardins P and Martel R 2009 The role of the oxygen/water redox couple in suppressing electron conduction in field-effect transistors *Adv. Mater.* **21** 3087–91
- [45] Kang H-S, Choi C-S, Choi W-Y, Kim D-H and Seo K-S 2004 Characterization of phototransistor internal gain in metamorphic high-electron-mobility transistors *Appl. Phys. Lett.* **84** 203506
- [46] Buscema M, Island J O, Groenendijk D J, Blanter S I, Steele G A, van der Zant H S J and Castellanos-Gomez A 2015 Photocurrent generation with two-dimensional van der Waals semiconductors *Chem. Soc. Rev.* **44** 3691–718
- [47] Fang H and Hu W 2017 Photogating in low dimensional photodetectors *Adv. Sci.* **4** 1700323
- [48] Konstantatos G, Levina L, Fischer A and Sargent E H 2008 Engineering the temporal response of photoconductive photodetectors via selective introduction of surface trap states *Nano Lett.* **8** 1446–50
- [49] LaPierre R R, Robson M, Azizur-Rahman K M and Kuyanov P 2017 A review of III–V nanowire infrared photodetectors and sensors *J. Phys. D: Appl. Phys.* **50** 123001
- [50] Kim J, Oh E, Xiao R, Ritter S, Yang Y, Yu D, Hee Im J, Hyuk Kim S, Jun Choi W and Park J-G 2017 Optical properties and bridge photodetector integration of lead sulfide nanowires *Nanotechnology* **28** 475706
- [51] Fang X, Xiong S, Zhai T, Bando Y, Liao M, Gautam U K, Koide Y, Zhang X, Qian Y and Golberg D 2009 High-performance blue/ultraviolet-light-sensitive ZnSe-nanobelt photodetectors *Adv. Mater.* **21** 5016–21